Numerical study of longitudinal vortex and chaotic flow on heat transfer characteristic in microchannels

Jincai Zhu, Ding Yuan*, Fan Sun, Yan'e Hu,

School of Mechanical and Electrical Engineering, Guangzhou Railway Polytechnic, Guangzhou 511300, China.

Corresponding author: Ding Yuan, Email: stu_yuand@163.com

Abstract

In this study, the flow characteristics and heat transfer mechanism of the chaotic flow induced by a microchannel containing staggered herringbone microstructures (CM), longitudinal vortex induced by a microchannel containing inclined ribs (SLM), and a smooth microchannel (SM) were comprehensively analyzed through numerical simulations at Reynolds number (*Re*) of 164 to 965. The results demonstrated that the primary enhanced heat transfer mechanism of the single longitudinal vortex was the disruption of the thermal boundary layer, whereas the chaotic flow enhanced heat transfer by facilitating fluid mixing. Furthermore, the longitudinal vortex decay is slower than that of the chaotic flow, resulting in SLM having a superior heat transfer performance at lower pressure drops compared with the CM. Further results showed that the SLM had the highest Nusselt number *Nu* (*Nu*=28), the best comprehensive evaluation factor (*PEC*) (*PEC*=2.1), and the lowest thermal resistance R_T (R_T = 0.6 K/W).

Keywords: Microchannels, Single longitudinal vortex, Chaotic flow, Heat transfer, Flow analysis.

1. Introduction

The microchannel heat sink was first proposed by Tuckerman and Pease in 1981 [1]. It has been widely used in microelectronic mechanical systems, chemical industry, energy, aerospace, and other fields owing to its high heat transfer efficiency and compact structure [2,3,4] With the development of high-performance, integrated, and miniaturized electronic devices, the heat flux in traditional integrated circuits has already exceeded 100 W/cm^2, and reached 10^3 W/cm^2 or even more in some ultra-large-scale integrated circuits. If the heat flux cannot be effectively removed, a rapid increase in temperature will reduce the reliability of electronic devices. Therefore, the pursuit of highly efficient heat-transfer heat sinks has emerged as a primary research focus for numerous scholars.

In recent years, scholars have conducted numerous studies on microchannels to further improve their heat-transfer performance. In general, technologies to improve the heat transfer performance of microchannels can be divided into active heat transfer enhancement technology and passive heat transfer enhancement technology. Active heat transfer enhancement technology requires external energy, such as external magnetic fields [5], electric fields [6], and surface vibrations [7], to achieve heat transfer enhancement. Passive heat transfer enhancement technology improves the heat transfer performance by changing the structure of the microchannels, using porous materials, or changing the coolant physical properties. Passive heat transfer enhancement technologies are widely used to enhance the heat transfer performance of microchannels, owing to their high reliability, economics, and applicability. With the benefit of this technology, many new microchannels have been developed in recent years, including divergent-convergent [8], wavy [9], and cavity-containing microchannels [10]. However, these microchannels have several shortcomings. For instance, the stagnation region may appear at low Reynolds numbers, which will have an unfavorable effect on heat transfer enhancement. To address these shortcomings, researchers have proposed the design of microchannels capable of inducing longitudinal vortices, chaotic flows, or other flow patterns to enhance heat transfer. For instance, Promvonge et al. [11] found that the presence of longitudinal vortexes induced by inclined ribs resulted in a maximum *PEC* of approximately 2.2. Apart from the increase in the Reynolds number, the significant increase in heat transfer was due to impingement jets induced by a longitudinal vortex pair of flow appearing on the upper, lower, and rib trailing end side walls. Feng et al. [12] demonstrated that the generation of longitudinal vortexes induced by wire coils enhanced the heat transfer performance in mini-channels effectively. Yuan et al. [13] observed that interconnected grooves effectively changed the flow transitioning from transverse vortices to longitudinal vortices, leading to higher heat transfer performance.

In the study of chaotic flows, researchers initially applied this flow to solve the problem of fluid mixing. However, it was discovered that chaotic flow also played a significant role in enhancing heat transfer. For instance, Greiner et al. [14] found that inducing chaotic advection in a system was one potential passive method for enhancing heat transfer. Stroock et al. [15] first comprehensively elucidated the enhancing mixing mechanism of the chaotic flow generated by staggered herringbone microstructures in their pioneering work. In addition, they indicated that chaotic flow also enhanced the rates of heat transfer because the mass transfer mechanism was closely related to that of the heat transfer. However, they did not analyze the pressure drop of the chaotic flow generated by staggered herringbone microstructures. Besides. researchers [16-17] also observed that chaotic flow occurred in various other configurations, such as wavy-walled microchannels and twisted patterns, and they concluded that they resulted in enhanced rates of mixing and heat transfer. Ghaedamini et al. [16] found that wavy walled microchannels were capable of inducing chaotic advection and strong chaotic advection was observed at high pressure drop. However, they found that strong chaotic advection may be achieved with smaller pressure drops in certain situations. Castelain et al. [17] observed completely regular chaotic flow (from the Eulerian point of view) experimentally in a twisted duct flow through a laser Doppler velocimeter (LDV). From the literature review, it is clear that both longitudinal vortices and chaotic flow can effectively improve thermal performance and comprehensive performance. However, these two types of flow are based on different mechanisms and exhibit different flow forms. As the fluid flow has a significant impact on the heat transfer performance, it is essential to investigate the influence of these two flows on the heat transfer and their fundamental differences.

In this study, staggered herringbones and inclined rib microstructures were selected to induce chaotic flow and longitudinal vortices. The thermal-hydraulic characteristics of the microchannels containing these two microstructures were numerically investigated. Thus, the effects of the longitudinal vortex and chaotic flow on the local thermal hydraulic characteristics (including distributions of local pressure drop, temperature fields, and dimensionless secondary flow intensity) and average thermal-hydraulic characteristics (including friction resistance coefficient, Nusselt number, and comprehensive performance under different Reynolds numbers) were analyzed thoroughly. This study will serve as a valuable guide for microchannel design to enhance heat transfer, particularly in the context of heat sink and transport phenomena.

2. Numerical simulation

2.1 Physical model

Fig. 1(a) shows the schematic diagram of the staggered herringbone microchannel (CM), with overall dimensions of 37 mm in length (L_s), 2.5 mm in width (W_s) and 1.25 mm in height (H_s). The fluid inlet section area of the CM was 1.5 mm in width (W_c) and 1.25 mm in height (H_c). The CM comprised three sets of microstructures, with each set containing six staggered herringbones, and the spacing (L_{S1}) between each set was 2 mm. The sizes of the staggered herringbone microstructures are 0.5 mm for the width (W_r) and 0.25 mm for the height (H_r). The distance (L_{S2}) between the two adjacent microstructures was 1 mm. The distance (L_{S2}) between two adjacent microstructures was 1 mm. The angle between the flowing direction and the microstructures was consistently 45°, as indicated by the green arrow. Fig. 1(b) shows a inclined ribs microchannel (SLM). Except the pattern of the SLM differs from that of the CM, the overall dimensions, fluid inlet section area, arrangement of the microstructures, and fluid flow direction remain consistent with those of the CM. Smooth rectangular microchannels (SM) were used for comparison with SLM and CM.

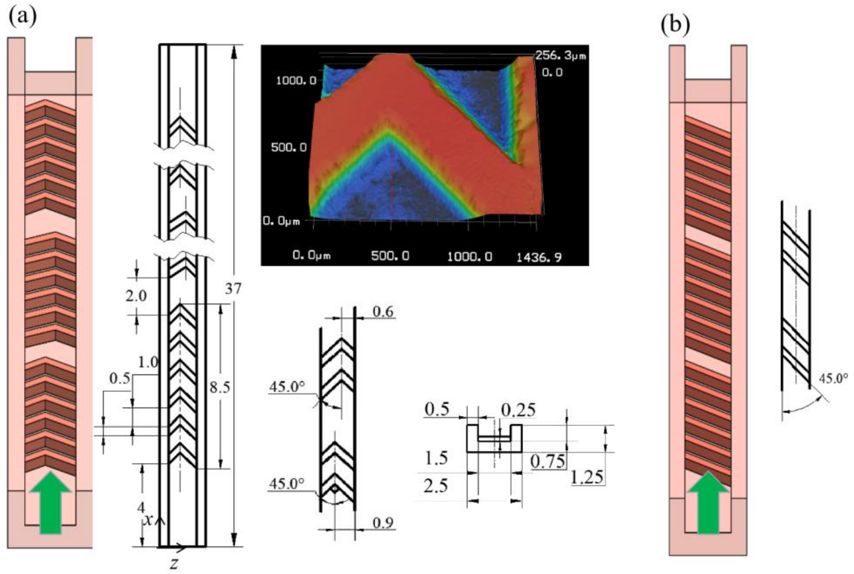

Fig. 1. Schematic diagrams of (a) CM and (b) SLM microchannel.

2.2. Numerical model

The numerical model can be assumed to be a three-dimensional steady-state incompressible laminar flow process, and the effects of volume force, gravity, thermal radiation and viscous dissipation can be ignored [12]. Under these assumptions, the governing equations were cited from Ref [12]. Copper and deionized water were chosen as the materials for the microchannel and coolant， respectively. The viscosity of deionized water was assumed to change in accordance with temperature fluctuations, and the specific expression was cited from Ref [18]:

The inlet flow rate of the coolant u_{in} was 0.12~0.84 m/s, and the temperature T_{in} was fixed at 298 K. A constant heat flux of $q_w=10^5$ W/m^2 was applied on the bottom of the microchannel. The remaining walls were assigned adiabatic walls and without velocity slip. Fluent CFD software was used to solve the model, with the convergence residual set as 10^{-5}.

2.3. Grid independence

Fig. 2 (a) and (b) show the grid structures of the SLM and CM. The SLM was used to determine the final grid number. As the deviations of pressure drops ΔP in the SLM corresponding to 0.8 and 1.8 million grids from that corresponding to 1.5 million grids were 7.2% and 2.3%, and the deviations of Nusselt number Nu of the SLM microchannel corresponding to 0.8 and 1.8 million grids from that corresponding to 1.5 million grids were 5.3 % and 1.5 %, respectively. The 1.5 million grid number was selected to divide all the microchannel geometric models. The discrepancy between the experimental and numerical mean Nu and ΔP of the SLM was validated in Section 3.1.

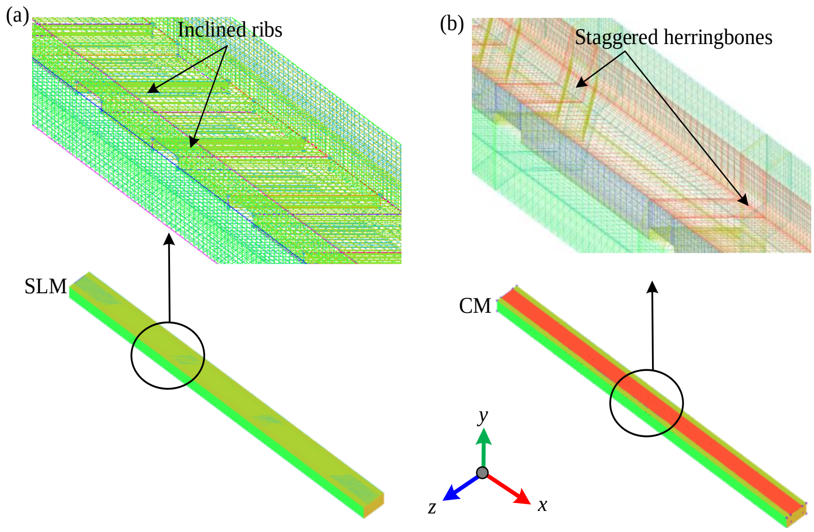

Fig. 2. Schematic diagrams of three-dimensional grid structure of (a) SLM, and (b) CM.

2.4. Data reduction

The formulas of Reynolds (*Re*), the hydraulic diameter of the microchannel (D_h),values of average Nusselt (*Nu*), the average Darcy friction resistance coefficient (*f*) , the pressure drop (ΔP) between the inlet and outlet, the comprehensive evaluation factor (*PEC*) and the thermal resistance (R_T), are cited from Ref [9].

To evaluate the intensity of the vortex in the cross section of the fluid, we defined the dimensionless secondary flow intensity *Se* as follows:

$$Se = \frac{\rho_f D_h^2 \frac{1}{A(x)} \iint_{A(x)} |\omega^n| dA}{\mu_f} \tag{1}$$

where ω^n and *A(x)* are the vorticity and the cross section of the fluid in the mainstream direction, respectively. The ΔSe is the difference between the *Se* and the Se_{Plain}, where *Se* and Se_{Plain} stands for the dimensionless secondary flow intensity in microchannels with and without microstructures, respectively.

$$\Delta Se = Se - Se_{\text{Plain}} \tag{2}$$

3. Results and discussion

3.1. Validation with experimental data

The discrepancy between the experimental and numerical mean *Nu* and ΔP values of the SLM was validated. The experimental setup was described in the authors' published paper [17]. The experimental conditions (cooling inlet temperature T_{in}, flow rate u_{in}, and heat flux q_w) were consistent with the simulated boundary conditions. The differences between the simulated results and tested data were within 5% and 6%, respectively, indicating that the numerical solution here was reliable.

3.2 Heat transfer characteristics

The variations in Nusselt number (*Nu*) and comprehensive evaluation factor (*PEC*) for different types of microchannels at different *Re* are given in Fig. 3(a) - (b), respectively. Fig. 3(a) shows that the *Nu* values of both the CM and SLM are significantly higher than those of the SM under the same *Re*, and the heat transfer performance of the SLM is better than that of the CM. Fig. 3(b) illustrates that the *PEC* values of both the CM and SLM are greater than 1. Furthermore, the *PEC* of the SLM surpasses that of the CM, indicating that the presence of staggered herringbones and inclined ribs has enhanced overall performance, with inclined ribs outperforming staggered herringbones.

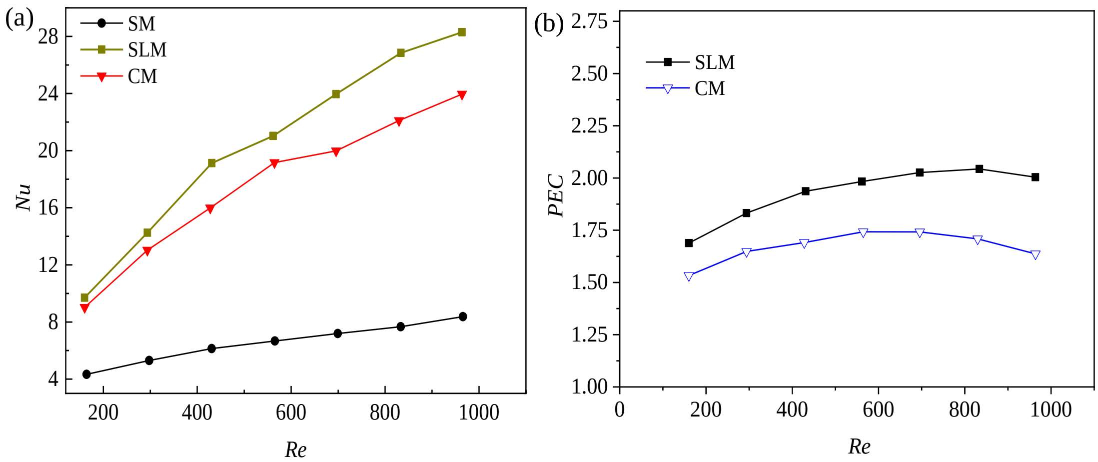

Fig.3. Heat transfer characteristics of different types of microchannels, variations in (a) Nusselt number (*Nu*), and (b) comprehensive evaluation factor (*PEC*) with different *Re* values.

3.3 Wall temperature analysis

Fig. 4 (a) depicts the T_{wx} curves of the SM, CM, and SLM in the *x* direction. It is evident from the figure that the T_{wx} of the CM and SLM exhibits a relatively gradual change trend, while the T_{wx} of the SM demonstrates a more pronounced variation compared to that of the CM and SLM. The temperature difference (ΔT_{wx}) at the inlet and outlet for the SM is 12.7 K, while it does not exceed 1.7 K for the CM and SLM. This suggests that the temperature uniformity of the CM and SLM is superior to that of the SM. Fig. 4(b) shows the thermal resistance R_T values of the SM, CM and SLM at different *Re* values. The R_T of the CM and SLM are much lower than that of SLM, which indicates that the heat transfer capabilities of the CM and SLM are stronger than that of the SM. The conclusion drawn from Fig. 4(b) is consistent with that of Fig. 4(a).

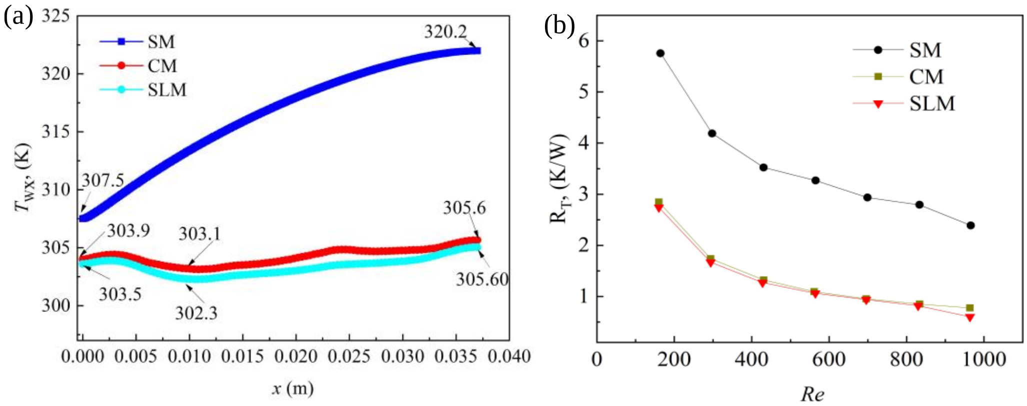

Fig.4. Wall Temperature T_{wx} along the *x* axis of the SLM, CM and SM at u_{in} =0.6 m/s.

Fig. 5 presents the wall temperature T_w contours on the heating wall for various microchannels. Specifically, Fig. 5 (a) contrasts the T_w of the SLM and CM. Fig. 5(a) demonstrates that T_w on the heating surface of the SLM distributed more evenly than that of the CM. Fig. 5 (b) provides the wall temperature T_w contour on the heating wall of the SM. The wall temperature difference between the inlet and outlet of the SM is significantly greater than that of the SLM and CM. This indicates that the heat dissipation capability of the SLM is marginally greater than that of the CM, and the heat dissipation capabilities of the SLM and CM are far greater than that of the SM. The analytical results of the wall temperature T_w in Fig 5 (a) and (b) are in accordance with the conclusions drawn from the wall temperature T_{wx} in Fig. 4(a) and the thermal resistance R_t in Fig. 4(b).

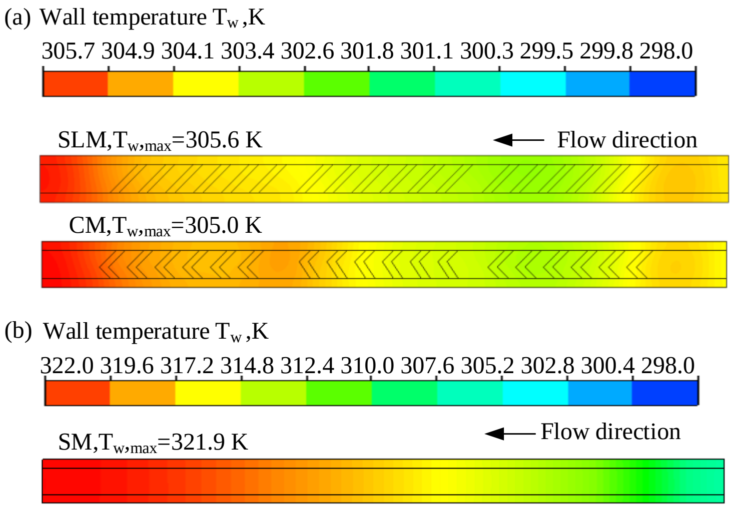

Fig.5. Wall temperature T_w contours of (a) SLM, CM and (b) SM, at u_{in} =0.6 m/s.

3.3 Analysis of heat transfer mechanism

The temperature gradient dT/dz of various types of microchannels thermal boundaries is analyzed to elucidate the heat transfer mechanisms in this section. A symmetric straight line crossing the solid domain, boundary layer and fluid domain is considered. Therefore, the line formed by point 1 (x=10 mm, y=0.8 mm, z=0) and point 2 (x=10 mm, y=0.8 mm, z=2.5 mm) are selected for this analysis, as shown in Fig. 6. It can be seen that the dT/dz values of all microchannels in both the solid and fluid regions are significantly smaller than those at the solid-fluid interface. The dT/dz in the solid region is equal to zero, because of its high thermal conductivity and uniform material. Similarly, all the dT/dz values in the fluid region are much lower than those at the solid-fluid interface. Meanwhile, the dT/dz values of the CM and SLM fluctuate, which is different from that of the SM. This is because the internal structures of the microchannels have an impact on flow and heat transfer. By contrast, the absence of microstructures in the SM ensures that there is no disturbance to the fluid, thereby maintaining a smooth dT/dz within the SM. Furthermore, it is observed that the fluctuation in dT/dz is more pronounced in the CM than in the SLM. This is attributed to the greater turbulence effect produced by the staggered herringbones compared with the inclined ribs. It also can be seen that the turbulence caused by the inclined ribs of the SLM predominantly impacts the solid-liquid interface, where a significant temperature gradient exists. In contrast, the turbulence generated by the staggered herringbones of the CM primarily affects the fluid region, where dT/dz is small. This leads to an increased heat transfer resistance and reduced heat transfer efficiency in the CM.

Fig. 6 illustrates that the maximum dT/dz values for the SM, CM, and SLM are located at the solid-liquid interface, with values of approximately 1.8×10^5 (K/m), 1.4×10^5 (K/m) and 0.4×10^5 (K/m) respectively. The maximum dT/dz values for the SM and CM are five and 3.5 times greater than that of the SLM, respectively. Additionally, it is observed that the boundary layer of the SM is the thickest, followed by that of the CM, with the SLM having the smallest boundary layer (as indicated by the black elliptic dotted line).

The above analysis clearly demonstrates that the disturbance effect of the SLM is primarily focused at the solid-liquid interface, resulting in a high heat transfer efficiency. On the other hand, the disturbance effect of the CM not only impacts the solid-liquid interface, but also extends to the fluid region. Consequently, the CM requires a greater pressure drop to enhance the heat transfer capacity.

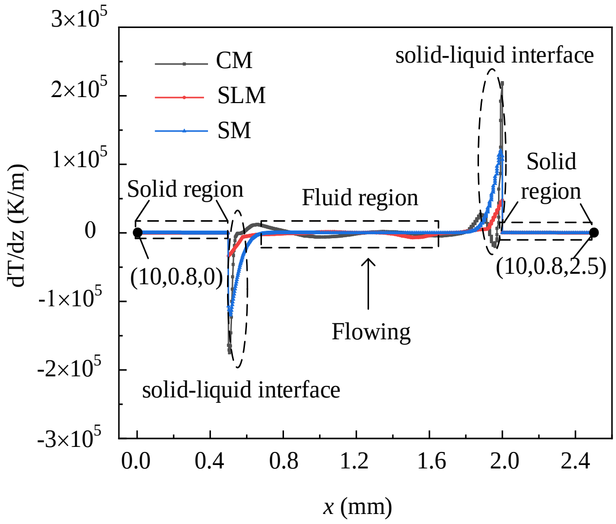

Fig. 6. Temperature gradients dT/dz of different types of microchannels at u_{in} =0.72 m/s.

3.4 Flow analysis

Fig. 7 shows the pressure drop (ΔP) and local pressure (p_x) as functions of *Re* for various microchannels. As shown in Fig. 7(a), the pressure drop ΔP values of the SLM and CM were significantly higher than those of the SM at the same *Re*. Compared with the SM, the ΔP of the CM and SLM increased more significantly with an increase in *Re*. This is attributed to the generation of chaotic flow and longitudinal vortices induced by the staggered herringbones and inclined ribs, which lead to additional mechanical energy consumption and increased fluid flow resistance. In addition, the ΔP values of the CM with staggered herringbones were found to be higher than those of the SLM with inclined ribs, indicating that the CM exhibited a higher flow resistance characteristic compared to the SLM. This is consistent with results shown in Fig. 6.

To better understand the influence of microstructures on the flow resistance, the axial variations in the local pressure (P_x) have been studied. As depicted in Fig. 7(b), it is evident that the P_x gradually decreases overall along the axial flow direction *x*.

However, there are fluctuations in P_x in some local fluid regions. For instance, the P_x suddenly drops at the inlet due to the entrance effect. Additionally, the P_x also fluctuates near the microstructures because of the sudden decrease in fluid velocity when impacting the microstructures. This leads to a slight increase in P_x as a result of the Bernoulli effect. It can be concluded that microstructure obviously affects the flow behavior of fluids and leads to pressure fluctuations. Meanwhile, when the fluid flows along the microchannels, the p_x decreases smoothly to zero at the outlet owing to the weakening and eventual disappearance of the vortex flow induced by the microstructures. Furthermore, it is evident that both the values and fluctuations of the P_x for the CM are greater than those of the SLM, indicating that a greater pressure drop is required for the fluid to,flow through the CM.

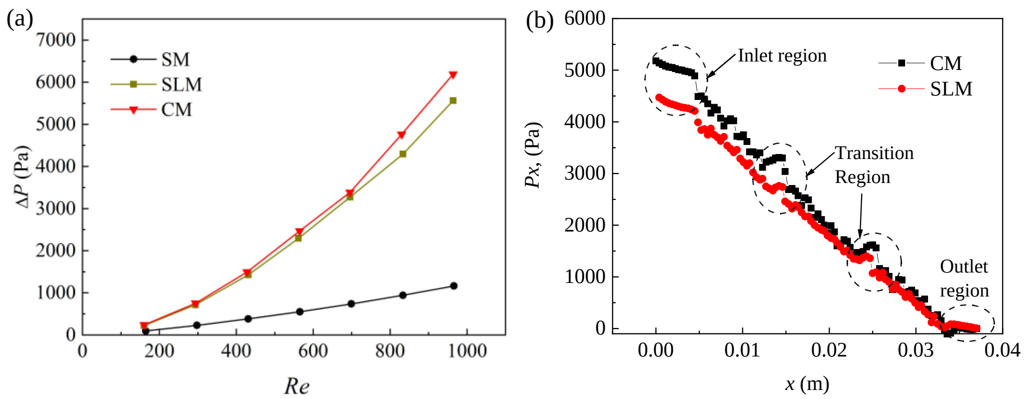

Fig. 7. Pressure drop of different types of microchannels, (a) ΔP with different Re, (b) axial variations of local pressure p_x at Re = 833, u_{in} =0.72 m/s.

Fig. 8 (a) depicts the changes in the friction resistance coefficient (f) of various types of microchannels with increasing Re. It is observed that both the CM and the SLM exhibit a gradual decrease in f as the Re increase, but the f of the CM remains higher than that of the SLM. Because f is directly proportional to ΔP, it can be concluded that ΔP for CM is greater than that for SLM at the same Re, resulting in a higher f value for the CM compared to the SLM. This suggests that the geometry of staggered herringbones is more intricate than that of the inclined ribs, leading to a more significant obstruction of fluid flow by the CM compared to the SLM.

Fig. 8 (b) illustrates the variation in the dimensionless secondary flow intensity ΔSe with respect to the x direction for both the SLM and CM. It is evident that the ΔSe of the CM is higher than that of the SLM, indicating that a greater pressure drop is required for fluid flow in the CM. The finding here agrees with that of the pressure drop analysis. In comparison to the CM, the variation of ΔSe in the SLM is more gradual, indicating that the longitudinal vortex induced by the SLM decays at a slower rate than that of the CM. This flow characteristic of the SLM enables it to achieve higher heat transfer performance at lower pressure drops.

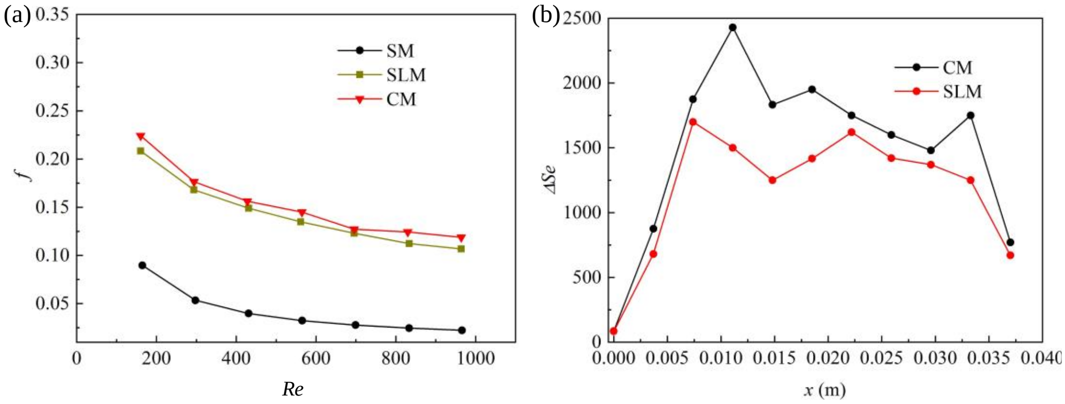

Fig.8. Flow characteristics of different types of microchannels, (a) *f* with different *Re*, (b) dimensionless secondary flow intensity ΔSe at Re = 833, u_{in} =0.72 m/s.

3. Conclusions

In this study, the flow and heat transfer characteristics of a chaotic microchannel CM and a single longitudinal vortex microchannel SLM were investigated. The essential differences in the heat-transfer mechanisms between the two microchannels were revealed. The main conclusions are as follows:

(1) The heat transfer resistance is mainly concentrated at the solid-fluid interface. Therefore, enhancing the disturbance of microstructures at the solid-liquid interface has a more pronounced effect than enhancing convection in the fluid region.

(2) The enhanced heat transfer mechanism of the SLM is inducing the fluid to impact the solid-fluid interface, rather than improving the convection of the central fluid, so as to obtain superior heat transfer performance.

(3) The longitudinal vortex decays more slowly than the chaotic flow, resulting in a higher heat transfer performance and lower pressure drop.

Declaration of competing Interest

All authors declare no competing financial interests to influence the work reported in this paper.

Acknowledgments

This work was supported by the Distinctive Innovation Project for Colleges and Universities of the Education Department of Guangdong Province (2023KTSCX310) and the Project of the Engineering Technology Development Center of Higher Education Institutions in Guangdong Province (Grant No. 2019GGCZX008).

References

[1] D.B. Tuckerman, R.F.W. Pease, High-performance heat sinking for VLSI[J], IEEE Electron Device Letters, 1981, 2(5):126-129.

[2] N.H. Naqiuddin, L.H. Saw, M.C. Yew, F. Yusof, T.C. Ng, M.K. Yew, Overview of micro-channel design for high heat flux application[J], Renewable Sustainable Energy Reviews,2018, (82):901-914.

[3] R.V Erp, R. Soleimanzadeh, L. Nela, G. Kampitsis, E. Matioli. Co-designing electronics with microfluidics for more sustainable cooling[J], Nature, 2020, 585(7824):211-216.
[4] L. Du, W.B. Hu. An overview of heat transfer enhancement methods in microchannel heat sinks[J] Chemical Engineering Science, 2023,119081.
[5] S.R. Hosseini, M. Sheikholeslami, M. Ghasemian, D.D. Ganji. Nanofluid heat transfer analysis in a microchannel heat sink (MCHS) under the effect of magnetic field by means of KKL model[J], Powder Technology, 2018, (324):36-47.
[6] N. Nourdanesh, F. Ranjbar, Investigation on heat transfer performance of a novel active method heat sink to maximize the efficiency of thermal energy storage systems[J], Energy Storage, 2022, (45): 103779.
[7] A.H.D.K. Rasangika, M.S. Nasif, W.P.R. Al-Waked, Numerical Investigation of the Effect of Square and Sinusoidal Waves Vibration Parameters on Heat Sink Forced Convective Heat Transfer Enhancement[J], Applied Sciences-Basel, 2022, 12(10): 4911.
[8] C.J. Ho, P.C. Chang, W.M. Yan, P. Amani, Efficacy of divergent minichannels on cooling performance of heat sinks with water-based MEPCM suspensions[J], International Journal of Thermal Sciences, 2018 (130):333-346.
[9] D. Yuan, W. Zhou, T. Fu, C. Liu, Experimental and numerical investigation ofheat and mass transfer in non-uniform wavy microchannels[J], International Journal of Thermal Sciences, 2020, (152):106320.
[10] T. Hou, Y. Chen, Pressure drop and heat transfer performance of microchannel heat exchanger with different reentrant cavities[J], Chemical Engineering and Processing-Process Intensification, 2020, (153):107931.
[11] Promvonge P, Tamna S, Kwankaomeng S, et al. Numerical investigation of laminar heat transfer in a square channel with 45° inclined baffles[J]. International Communications in Heat and Mass Transfer,2010, (37): 170-177.
[12] Z.F. Feng, X.P. Luo, F. Guo, H.Y Li, J.X Zhang, Numerical investigation on laminar flow and heat transfer in rectangular microchannel heat sink with wire coil inserts[J], Applied Thermal Engineering, 2017, (116):597-609.
[13] D. Yuan, W. Zhou, T. Fu, Q.Y Dong. Heat transfer performance of a novel microchannel embedded with connected grooves[J], Chinese Journal of Mechanical Engineering, 2021, 34(1):145.
[14] M. Greiner, G.J. Spencer, P.F. Fischer, Direct numerical simulation of three dimensional flow and augmented heat transfer in a grooved channel[J], Journal of Heat Transfer-Transactions of the ASME, 1998, 120 (3): 717-723.
[15] A.D. Stroock, S.K. Dertinger, A. Ajdari, I. Mezic, H.A. Stone, G.M. Whitesides, Chaotic mixer for microchannels[J],Science, 2002, 295(5555): 647-651.
[16] H. Ghaedamini, P.S Lee, C.J Teo, Enhanced transport phenomenon in small scales using chaotic advection near resonance[J], International Journal of Heat and Mass Transfer,2014, (77): 802-808.
[17] C. Castelain, A. Mokrani, Y.L. Guer, H. Peerhossaini, Experimental study of chaotic advection regime in a twisted duct flow[J], European Journal of Mechanics B-Fluids, 2001, 20(2): 205-232.
[18] Z. Dai, Z. Zheng, D.F. Fletcher, B.S. Haynes, Experimental study of transient behaviour of laminar fow in zigzag semi-circular microchannels[J], Experimental Thermal and Fluid Science, 2015, 68: 644 – 651.

Submitted: 18.06.2024.
Revised: 28.06.2024.
Accepted: 08.08.2024.